Modeling and Experimental Analysis of the Mass Loading Effect on Micro-Ionic Polymer Actuators Using Step Response Identification

Iman Dadras, Sofiane Ghenna, Sébastien Grondel, Éric Cattan, Jaan Raik, Alvo Aabloo, *Member, IEEE*, and Saoni Banerji

***Abstract*— This paper presents a linear electrochemomechanical model for microscale ionic actuators. A frequency-domain approach is used to facilitate model interpretation, simplify model application, and accelerate the generation of actuator-specific models. A system comprising a micro PEDOT:PSS/PEO actuator with external loading at its tip was modeled to incorporate the mass loading effect using the proposed approach. Analysis showed that the simulation results of the reported model were in agreement with the experimental measurements conducted with variability in the mass and input voltage. The success of the proposed modeling approach promises to enable its application in the control of microscale ionic actuators for potential biomedical applications. [2020-0388]**

***Index Terms*— Ionic EAP, analytical model, system identification, mass loading effect, frequency domain.**

I. Introduction

INSPIRED by biological systems, soft robots show reduced complexity and higher adaptability in their interactions with the environment [1]. Using unconventional materials that embed sensing and control architectures allows robots to mimic the incredible capabilities of biological organisms in complex tasks [2]–[4] and exhibit higher bending and twisting capabilities in constrained environments than their conventional rigid-bodied counterparts [5], [6]. In recent years, ionic electroactive polymer-based actuators (IEAPs) have attracted global interest among scientists. IEAPs are believed to have potential utility in biomedical applications [7], [8], such as steerable microcatheters [9], [10], microscopy [11], drug delivery [12]–[16], position-controlled microinjection [17], imaging [18], and microsurgical tools [19].

Manuscript received December 18, 2020; revised February 3, 2021; accepted February 18, 2021. Date of publication March 2, 2021; date of current version March 16, 2021. This work was supported by the Institute of Technology basic funding grant 20907, H2020 project TWINNIMS (Grant agreement 857263), Estonian Research Council Grant 772 and Estonian Centre of Excellence in ICT Research. Subject Editor I. Dufour. *(Corresponding author: Iman Dadras.)*

Iman Dadras, Alvo Aabloo, and Saoni Banerji are with the Intelligent Materials and Systems Laboratory (IMS Laboratory), Institute of Technology, University of Tartu, 50411 Tartu, Estonia (e-mail: iman.dadras@ut.ee).

Sofiane Ghenna, Sébastien Grondel, and Éric Cattan are with the Université Polytechnique Hauts-de-France, CNRS, University of Lille, YNCREA, Centrale Lille, UMR 8520-IEMN, DOAE, 59313 Valenciennes, France (e-mail: eric.cattan@uphf.fr).

Jaan Raik is with the Department of Computer Engineering, Tallinn Technical University, 12618 Tallinn, Estonia (e-mail: jaan.raik@taltech.ee).

Color versions of one or more figures in this article are available at https://doi.org/10.1109/JMEMS.2021.3060897.

Digital Object Identifier 10.1109/JMEMS.2021.3060897

Among the ionic actuators that operate in air [20] and host their ionic liquid [21], [22], poly (3,4 ethylene dioxythiopene) (PEDOT)-based actuators have received considerable attention due to their low density, biocompatibility [23], high reversible, and fast-switching redox processes [24]. Additionally, these actuators have a long life cycle (7×10^6 cycles at f = 10 Hz) without delamination or degradation [25] and require low operating voltages (typically $\leq$ 3 V) [26] and a low frequency bandwidth (0.01 Hz-0.5 Hz) [27]. Due to these advantages, PEDOT-based actuators are promising candidates to enable a wide range of microscale applications [25], [28]. To fully realize the potential of these materials, a novel reproducible clean-room compatible process has been demonstrated for fabricating trilayer actuators by stacking each layer sequentially and obtaining an interpenetrated architecture [29] (Fig. 1(a)) with integrated electrically contacting solutions (Fig. 1(b)) [28], [30]. This process removes the need for manual handling, making the fabrication of such actuators highly automated, which, in turn, enables short device lengths and thin layers for faster actuation [27], [30]. For such a configuration, the central layer acts as an ionic host matrix for the electrolyte and as an ion transfer membrane. This matrix is formed of an interpenetrated polymer network (IPN) composed of two cross-linked polymers—poly(ethylene oxide) (PEO) and nitrile butadiene rubber (NBR). IPN is the electronic separator between two working electrodes made of a conducting polymer—PEDOT. The obtained trilayer is filled with the ionic liquid 1-ethyl-3-methylimidazolium bis-trifluoromethyl sulfonyl-imide (EMImTFSI) [20], [22]. Upon excitation of a (bipolar) electrical potential between the electrodes, a redox (reduction/oxidation) process occurs in the conducting polymer, resulting in the mass transport of ions. This primary mechanism is responsible for the volumetric variation of these electrodes, leading to their actuation capability.

Modeling is critical for understanding and analyzing the coupled electrochemical-mechanical aspects and predict the behavior of such actuators in many of their intended applications, such as endoscopy, microsurgery, and manipulation. To our knowledge, few models for such a family of actuators have been developed to date. Existing methods of modeling conducting polymer-based actuators rely on one of the three categories. White-box models [31], [32] are based on physical principles that capture the system's fundamental physics through analytical methods. The system internals are fully

known and provide an exact solution to the problem; however, they are complex and are not suitable for real-time control. Black-box models [33], [34] are based on data mapping, in which a transfer function is usually built from experimental data. Such models are simple and suitable for real-time control; however, they provide minimal insight into the governing mechanisms present in the system and hence have limited application. On the other hand, gray-box models [7], [35] are a trade-off between white-box and black-box models [27]. These models are partly based on physical principles and empirical measurements, thus bridging the gap between physics-based and systems theory.

In the context of the presented work, few notable works on gray-box models for such a family of actuators are reviewed. For example, Bentefrit *et al.* [36] presented a linear electrochemomechanical model using the bond graph finite difference method [37] to simulate the behavior of ionic trilayer actuators while visualizing the energy and power efficiencies along the actuator length and over time. Nguyen *et al.* [38] advanced existing work by implementing a nonlinear dynamic model incorporating mechanical inertial effects. The model provides a deeper understanding of the nonlinear behavior of such actuators that stems from the changes that occur as the voltage is increased [39]. Punning *et al.* [40] presented a scalable distributed model of ionic polymer-metal composite (IPMC) actuators as a lossy resistive-capacitive (RC) transmission line to model the changing curvature. This distributed nature of the model allows modeling of the nonuniform flexion of the material in the space and time domains. However, it does not take into account the mechanical parameters of the IPMC membrane, such as the inertia and viscoelasticity of the polymer membranes. This model was improved by Vunder *et al.* [41] by incorporating the back relaxation of IEAPs and extending it in different IEAP materials. By utilizing distributed port-Hamiltonian systems (PHS), Nishida *et al.* [42] present a versatile model for IPMC actuators based on boundary multiscale coupling, allowing them to analyze the influence of local and nonuniform properties. In the studies mentioned above, models have been derived to deepen the understanding of actuator behavior alone, without considering its interaction with the structure it intends to set in motion, for example, their use in potential biomedical applications, such as micromanipulation, microscopy, and catheterization.

In this category, we can quote the work of Mattioni *et al.* [43], who developed a lumped scalable model and control strategy using PHS formalism to reproduce the basic mechanical properties of an IPMC-actuated compliant biomedical endoscope. The implemented control strategies successfully enable the desired equilibrium configuration and dynamic behavior to be achieved. Shoa *et al.* [44] presented a dynamic electrochemical and mechanical model for predicting the bending and actuation rate of a conducting polymer actuator-driven structure for its intended use in intravascular imaging. The delay associated with the finite electronic resistance across the polymer length was taken into account to accurately model the transient response. An analytical bending curve model dedicated to nano/micromanipulation applications was implemented by Alici *et al.* [45]. The static characteristics of the conducting polymer actuators were employed to enable accurate prediction of the actuation under different applied potentials.

Other interesting applications for performing medical diagnosis require such actuators to move an external load, such as a camera. The introduction of a weight force component alters the equilibrium of the system, on the whole. In other words, while the coupled electrochemical and mechanical domains govern the bending moment and curvature of the actuator, the mechanical force produced due to the addition of an external load has a significant impact on the actuator's tip deflection and curvature. As this force component is coupled with the electrochemomechanical behavior, one cannot predict the curvature of the actuator by only applying the superposition of forces. Therefore, a model is required to incorporate the coupling of the electrochemical and mechanical domains, together with mass loading effects

The present work is dedicated to predicting and understanding the effect of mass loading at the tip of a micro IEAP actuator. The payload weight can be handled as a system disturbance. This disturbance can cause a steady-state error and alter transient-response specifications. Although these performance deteriorations are compensable by applying higher-order closed-loop control systems, having the loading effects already considered in the actuator model leads to simpler control and better performance [46].

An actuator based on PEDOT:PSS/PEO as the conducting polymer, loaded and unloaded, is studied in terms of its curvature under an applied voltage and in the frequency domain. With the partial knowledge of the electrochemical phenomena occurring in the actuator, a simple linear gray-box model based on a lumped-parameter approach is developed to predict the actuator behavior in the frequency domain. Actuator-specific model generation with gray-box models analyzed in the time domain requires numerous measurements to determine the electrical (electrode resistance, series resistance, leakage resistance, and double-layer capacitance) and mechanical (Young's modulus and damping ratio) specifications [36], [41]. The primary benefits of such a model lie in first employing a simple approach for acquiring the necessary actuator specifications from its step response as time constants and a gain in the frequency domain. Second, driving differential equations in the time-domain approach are substituted by straightforward Laplace-domain algebraic transfer functions facilitating the application of the model for different inputs and initial values, consistent with interacting electrical and mechanical systems models. Third, a more concise model representation in the frequency domain eases model interpretations using Bode plot or s-plane graph analysis. Additionally, by modeling the payload weight as a feedback and calculating the closed-loop transfer function, the frequency-domain model is extended to include the mass loading effects. Finally, robust system analysis tools in the frequency domain enable the system stability to be evaluated for different payload masses.

The article is organized as follows. Section II outlines the methodology adapted to develop the proposed linear model for a mass loaded actuator and provides a brief review of the physical equations coupled in each domain. In Section III,

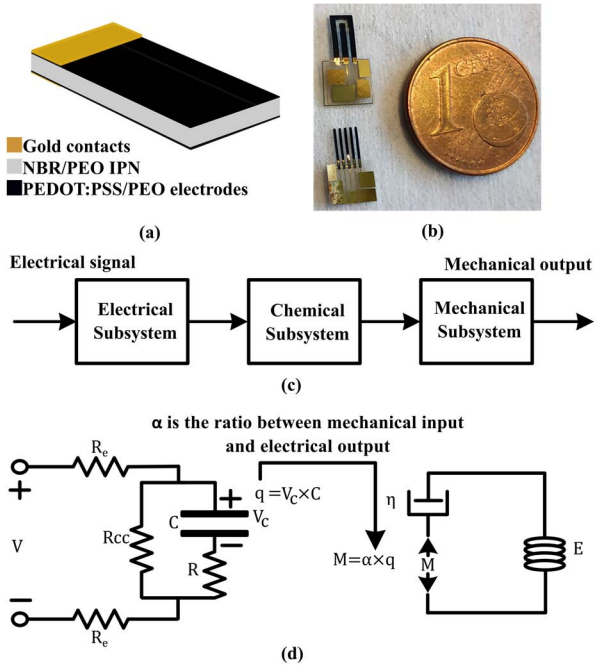

Fig. 1. (a) 3D view of the PEDOT:PSS/PEO actuator structure (b) Prototypes incorporating PEDOT:PSS/PEO micro-actuators with integrated gold contacts. (c) Coupled subsystems of an ionic actuator (d) Equivalent circuit of an ionic actuator.

the actuator curvatures are experimentally recorded and validated by varying the weight of the external loads and changing the applied voltage. An interpretation of the results and sources of error is discussed in Section IV, focusing on the employed approach followed by concluding remarks in Section V.

II. Presentation of the Model

In this section, according to the driving linear differential equations of IEAP actuators, their Laplace transfer function is introduced. The transfer function is split into separated electrical, chemical, and mechanical subsystems. Then, the payload weight is modeled as a feedback block on the mechanical subsystem and a new mechanical input.

A. Electro Chemo-Mechanical Aspect

Ionic actuators can be represented as a system with an electrical input (mostly expressed by voltage or current) and a mechanical output (usually described as a curvature or displacement).

A generic linear gray-box model of an ionic actuator divides the actuator into three subsystems: electrical, chemical, and mechanical (Fig. 1(c)) [36], [41]. For the electrical part, actuators act as networks of capacitors and resistors upon application of a voltage at low frequencies. From a mechanical perspective, they are modeled with cantilever beams for small deflections. The actuators' electrical and mechanical subsystems are elaborately modeled by their corresponding elements, whereas the chemical subsystem is substituted by a ratio that relates the output of the electrical part (mainly electric charge (q) stored in the actuator's electric double-layer capacitor) to the mechanical part input, e.g., the bending moment (M). The input electrical voltage charges the double-layered capacitor through an RC network. This ionic charge transport causes a proportional bending moment in the actuator. The resulting bending moment bends the actuator (see Fig. 1(d)). In Fig. 1(d), R is the series resistance of the double-layer capacitor, C; q is the electric charge stored in the capacitor; Re models the electrode resistance; and Rcc represents the leakage resistance. On the mechanical side, E and I represent the Young's modulus and second moment of inertia, respectively. The chemical subsystem is modeled by the ratio of the bending moment to the electric charge, as shown by α.

To analyze the actuator in the frequency domain, the transfer functions of these electrical and mechanical subsystems are required. The transfer function is driven by the differential equation explaining the relationship among the voltage (V), q, M, and curvature (κ). These relationships are demonstrated in [41] and are given in (1) and (3).

$$q(t) = e^{-\frac{1}{RC}t}\left(\int_0^t \frac{V(\tau)}{R} e^{\frac{1}{RC}\tau} d\tau\right) \tag{1}$$

In [41], to consider the voltage drop alongside the actuator length, the actuator is modeled as a lossy RC transmission line through which the voltage and subsequently $q(t)$ decrease. However, the low resistance of the actuator electrodes (Re) used in this work (the resistivity of the electrode is 62.5 $\mu\Omega$.m) abates the voltage drop along the actuator's length. Thus, the transmission line model is not necessary, and the electric charge in this paper is only a function of time. Neglecting the transmission line and Re as explained, Rcc is only important to energy consumption and heating, which are both outside the scope of this paper. Therefore, the effect of Rcc is negligible in this work.

The transfer function of the electrical subsystem is obtained from the Laplace transform of (1):

$$\frac{Q(s)}{V(s)} = \frac{\frac{1}{R}}{s + \frac{1}{RC}} \tag{2}$$

In the above equation, s is a complex number frequency parameter. From [41], the differential equation of the mechanical subsystem is expressed as follows:

$$\kappa(t) = \mu[q(t) - \lambda e^{-\lambda t} \int_0^t q(\tau) e^{\lambda \tau} d\tau] \tag{3}$$

$\mu = \alpha/EI$ is the coefficient that relates curvature to the charge. $\lambda = E/\eta$ denotes the rate of relaxation. η represents the viscosity [41].

The mechanical subsystem transfer function is derived from (3) and denoted in (4).

$$\frac{\mathrm{K}(s)}{Q(s)} = \frac{\mu s}{s + \lambda} \tag{4}$$

However, the desired transfer function in this paper is expressed as $K(s)/M(s)$ because feedback occurs on the mechanical subsystem. Thus, via the substitution of $M(t) = \alpha q(t)$ in (4), the mechanical subsystem transfer function is acquired.

$$\frac{\mathrm{K}(s)}{M(s)} = \frac{\frac{1}{EI}s}{s + \lambda} \tag{5}$$

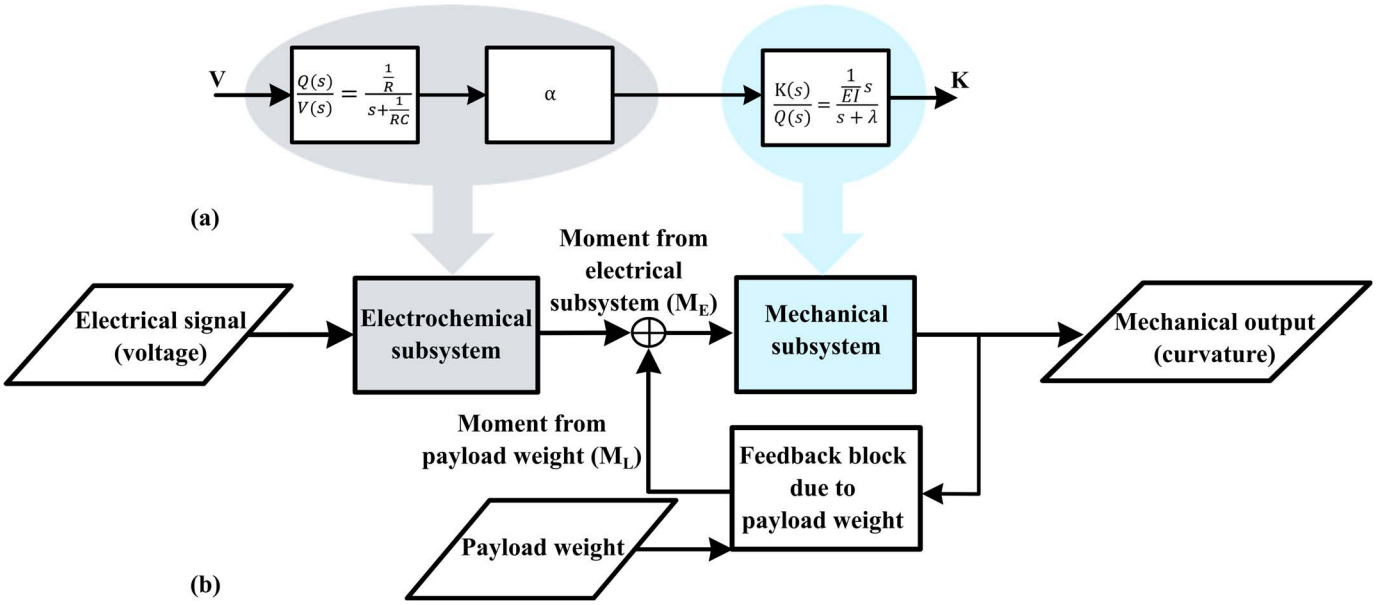

Fig. 2. Block diagram of the ionic actuator (a) Unloaded: subsystems with their relative transfer functions (b) Loaded: payload effect modeled as a feedback block.

The block diagram of the unloaded actuator with the computed transfer function is depicted in Fig. 2(a).

B. Loading Aspect

The model that describes the effect of the payload at the tip of an ionic actuator is presented here. The weight of this payload (W) adds a new input to the system, in addition to the electrical input. Depending on the orientation and curvature of the actuator, a component of the payload weight is in the bending direction. Hereafter, this component is called the effective force (F_e). The effective force causes an additional bending moment and curvature in the actuator. Therefore, the effective force depends on and results in curvature. A feedback loop between the mechanical output (curvature) and input (bending moment) is formed (Fig. 2(b)). The remainder of this paper elaborates on this idea using an application case.

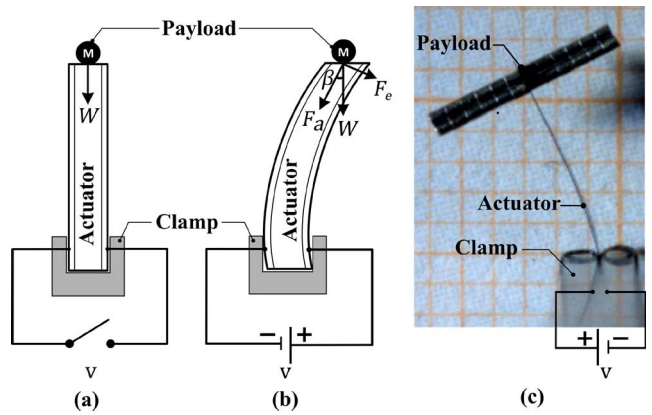

Fig. 3. System configuration of a loaded actuator (a) without and (b) with applied voltage. (c) PEDOT:PSS/PEO actuator bending in response to the application of 2 V input and a payload mass (magnets) of 12.6 mg.

C. Global Model

1) System Configuration and Assumptions: In this section, the implementation of a feedback loop is incorporated in the loaded actuator's mechanical subsystem to model the effect of the payload weight on the actuator. A specific configuration is studied in this context. The configuration consists of an actuator and a payload attached to one end of the actuator (actuator tip). The orientation of the system is vertical, and the length of the actuator is parallel to the gravitational field. Fig. 3 shows the configuration of the actuator, in which one end of the actuator is secured at a fixture. The payload weight has no effective component before actuation (Fig. 3(a)), whereas Fig. 3(b) shows the effective force component of the payload weight on an actuator when driven by an electrical signal. This component causes more bending in the same direction. Therefore, positive feedback exists in the mechanical subsystem. The ratio between F_e and W is equivalent to the sine of the angle between the gravitational field and the actuator tangent ($F_e = Wsin(\beta)$). Although the curvature caused by the bending moment resulting from the payload weight increases as it moves further from the actuator tip, the actuator throughout its length can be approximated as an arc with a constant curvature equal to the average actuator curvature. In this case, β and the central angle of this arc are complementary to the angle between W and F_e. Therefore, β is equal to the central angle and is calculated by the product of κ and the actuator length (l) ($\beta = \kappa l$). Another assumption is that the axial force (F_a) does not compress the actuator length. The bending response of a PEDOT:PSS/PEO actuator in response to a voltage input with an amplitude of 2 V_{pk-pk} (opposite polarity) and a payload mass of 12.6 mg is shown in Fig. 3(c).

2) Feedback Loop and Derivation of the Closed-Loop Transfer Function: The payload weight creates a feedback loop in the mechanical subsystem. The bending moment caused by F_e on the actuator is calculated by $M = F_e d$. In this equation, d is the distance from the payload on the actuator, which means that M and κ resulting from loading

TABLE I
FEEDBACK AND MECHANICAL INPUT FOR DIFFERENT CURVATURES

Region	Angle (Radian) (κl_e)	M_e (N.m)	Feedback (N.m^2)	Mechanical input M_l (N.m)
1	$\kappa(t)l_e < -1.05$	$mg\frac{2l_e}{3}(-0.6 + 0.24\kappa l_e)$	$0.24mg\frac{2l_e^2}{3}$	$-0.6mg\frac{2l_e}{3}$
2	$-1.05 < \kappa l_e < -0.55$	$mg\frac{2l_e}{3}(-0.14 + 0.7\kappa l_e)$	$0.7mg\frac{2l_e^2}{3}$	$-0.14mg\frac{2l_e}{3}$
3	$-0.55 < \kappa l_e < +0.55$	$mg\frac{2l_e}{3}l_e\kappa$	$mg\frac{2l_e^2}{3}$	0
4	$0.55 < \kappa l_e < 1.05$	$mg\frac{2l_e}{3}(+0.14 + 0.7\kappa l_e)$	$0.7mg\frac{2l_e^2}{3}$	$+0.14mg\frac{2l_e}{3}$
5	$\kappa(t)l_e < -1.05$	$mg\frac{2l_e}{3}(-0.6 + 0.24\kappa l_e)$	$0.24mg\frac{2l_e^2}{3}$	$+0.6mg\frac{2l_e}{3}$

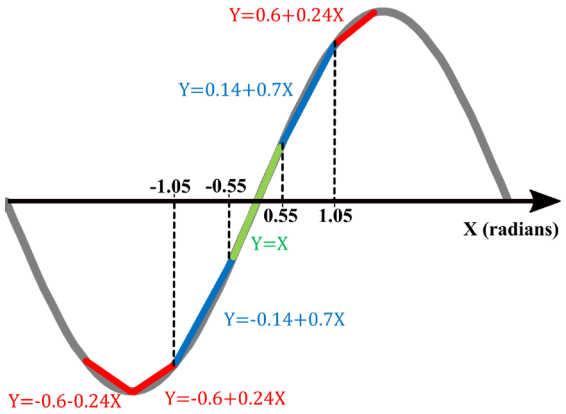

Fig. 4. Linearization approach (sine function linear approximation).

are increasing along the actuator length from the actuator tip to the fixed end. However, in this paper, for simplicity, the entire actuator is represented by an arc with a constant curvature passing the fixture and the position of the actuator tip. To adhere to this representation, the tip force (F_e) should be substituted by a constant bending moment (M_e) that gives the same deflection at the actuator tip. M_e is calculated in (6). Due to technical difficulties, it is not possible to attach the payload to the very tip of the actuator. Additionally, a part of the actuator is under electrical contact. Therefore, the distance between the payload and the fixed end is slightly less than the actuator length. As this distance is of interest here and should not be confused with the geometric length of the actuator, the length between the payload mass center and the fixed end of the actuator is called the actuator effective length (l_e).

$$M_e = \frac{2}{3}l_e F_e \tag{6}$$

In this application case, $\beta = \kappa l_e$, and thus, $F_e = Wsin(l_e\kappa)$. Therefore, the payload weight causes a feedback via a sine function. As our goal is a linear model in this paper, the sine function should be linearized. Fig. 4 shows the linearization approach applied in this work.

Therefore, the approximation of F_e for different angles consists of a constant and a curvature dependent component. The constant is modeled as a mechanical input, whereas the coefficient of the output κ in the dependent component is the feedback. Table I shows the effective bending moment (M_e), feedback, and mechanical input (M_l) for different output values. In this table, m is the mass of the payload, and g is the acceleration due to gravity.

III. MODEL VERIFICATION: MATERIALS AND METHODS

A. Beam Synthesis and Experimental Setup

The fabrication process of the microactuators was done by sequential layer stacking Fig. 1 (a) and (b). Two PEDOT:PSS electrodes with PEO network precursors were fabricated using the casting method. They were placed above and below a spin-coated layer of a semi-interpenetrating polymer network precursors. This last layer was composed of PEO network and nitrile butadiene rubber. Different annealing steps were performed to finalize polymerization. The details of the fabrication procedure are described in [28], [30]. These steps allow precise control of the thickness of every layer because the volume of the casted solution and the rotation speed of the spin-coater can be easily adjusted. In the last step, the microbeams of the actuator were obtained via the laser ablation technique and were swollen in EMImTFSI before further characterization. The characterized microbeams studied in this work had dimensions of 6000 × 1374×35 μm with an effective mass of 0.695 +/- 0.004 mg.

To observe the high amplitude motion of the microbeams actuated at different voltages, a Phantom Miro LC high-speed camera (from Vision Research) was used. This camera allows the recording of 3200 frames per second (fps) at 12-bit depth with a full resolution of 1280 × 800 pixels [47]. Since the microbeam's working frequency is 0.1 Hz, only 24 fps were used with a resolution of 640 × 480 pixels. We then obtained at least 240 frames per microbeam's motion cycle and therefore studied its curvature at different positions. A lighting solution [48] with a maximum light output of approximately 108.000 lx/50 cm was also added with a reflecting panel to ensure appropriate light exposure, as required for this kind of recording.

B. Determination of the Parameters

1) System Identification: For system identification, an unloaded actuator was excited by 0.1 Hz square wave voltage inputs with amplitudes of $2V_{pk-pk}$ and $3V_{pk-pk}$. The actuator's curvature was recorded, and the repeatability in its motion was verified. As the step response is of interest, a half cycle of the actuation to the $3V_{pk-pk}$ input was analyzed and fitted to a second-order linear time-invariant (LTI) system

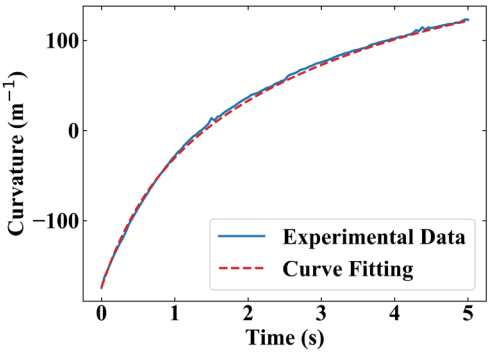

Fig. 5. System identification by fitting the measured actuator step response to a second order LTI system step response (unloaded).

step response (see Fig. 5). The equation for the second-order fitting in Fig. 5 is expressed as follows:

$$\kappa\,(t) = 181 - 90e^{-1.8t} - 265e^{-0.3t} \tag{7}$$

The above equation is the response of the system with an initial value of $\kappa\left(0^{-}\right) = -174$ to the input of $V = 3u(t)$, where $u(t)$ is the Heaviside step function. Therefore, the transfer function of the actuator is calculated as follows:

$$\frac{\mathrm{K}\,(s)}{V(s)} = \frac{63(s+0.52)}{(s+0.3)(s+1.8)} \tag{8}$$

A comparison among (8), (5) and (2) leads to the conclusion that the zero- and low-frequency poles belong to the mechanical subsystem, and the high-frequency pole is related to the electrical subsystem. Since the feedback loop is formed on the mechanical subsystem, this subsystem is especially of interest. To completely identify the mechanical subsystem, the gain of this block should also be known.

2) Mechanical Subsystem Gain: The mechanical subsystem gain is derived as $\frac{1}{EI}$. However, the Young's modulus is only valid for small deflections when the actuator is undergoing elastic deformation. The observed deflection is high in the conducted experiments, and the stress is even higher in the area close to the fixed end. Out of the linear elasticity region, the stress-strain relationship is complicated. The stress varies throughout the actuator length due to the payload weight and over time by actuation. Therefore, using the stress-strain equations is impossible in a nondistributed linear model.

Furthermore, the Young's modulus changes with the applied voltage [38]. Thus, the Young's modulus cannot be used in this paper because the voltage changes over time. Instead, an empirical mechanical subsystem gain is used.

The mechanical subsystem gain is chosen as the model with the average or most popular payload weight, and the input voltage has zero error. The mechanical subsystem gain is obtained as $4.86 \times 10^{7} N^{-1}.m^{-2}$.

C. Model Verification

A set of six experiments were conducted with three different payload masses, 3.15 mg, 6.30 mg, and 12.60 mg, and two input voltage amplitudes, 2 V_{pk-pk} and 3 V_{pk-pk}, to verify the model with a variable mass and input voltage.

The values of the initial curvature and effective length for different payload masses (m) are given in Table II.

TABLE II
EXPERIMENTS: PARAMETERIZATION AND SPECIFICATIONS

m (mg)	l_e (mm)	$\kappa(0^{-})$ (m^{-1})	
		2 V	3 V
3.15	6.20	-133	-132
6.30	6.7	-156	-241
12.60	6.27	-209	-303

TABLE III
VALIDATION OF THE PROPOSED MODEL

Experiment	P_P κ (m^{-1})	P_P Error	% Error
a	243	25	10
b	248	5	2
c	260	37	14
d	263	11	5
e	428	60	14
f	504	75	14

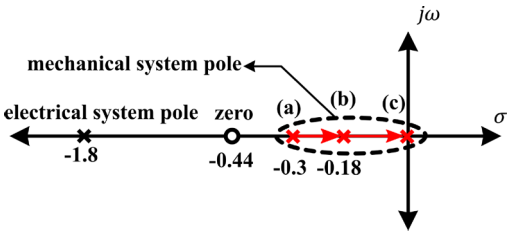

Fig. 6. System stability analysis: location of the actuator poles and zero. Mechanical subsystem pole for (a) an unloaded actuator, (b) a payload mass = 12.6 mg, and (c) marginal stability, calculated with a payload mass = 20 mg.

According to the values for l_e and the initial curvature for the experiment conducted with an applied voltage of 3 V and a 12.6 mg load, the actuator is in Region 1 of Table I. Thus, after calculating the closed-loop transfer function of the system, the responses to the electrical and mechanical inputs and zero input were calculated. It should be noted that as the mechanical input stays unchanged from the previous cycle, this input is constant (see Fig. 4Fig. 4). The obtained response is valid until the curvature reaches a value at which the system conditions are placed under Region 2. After adding a feedback to the transfer function, the three responses, electrical, mechanical, and zero input, were calculated. In this region, as the mechanical input changes from $-0.6mg\frac{2l_e}{3}N.m$ to $-0.14mg\frac{2l_e}{3}N.m$, the mechanical input is $(-0.6 + 0.46u(t - t_1))mg\frac{2l_e}{3}N.m$, where t_1 is the transition time from Region 1 to Region 2. Additionally, the initial curvature for each region is the curvature at the transition time to that region. This procedure is repeated for Regions 3-5.

Fig. 7 shows the alignment of the measured curvatures and simulation results obtained from the model. The results show a close convergence between the model simulations and the measurements. An in-depth analysis of the convergence is detailed in Section IV.

D. Stability Analysis

As the linear approach presented in this paper is best suited for small curvatures, stability analysis is conducted for Region 3. The actuator pole and zero locations are shown in the s-plane in Fig. 6. As the payload mass increases,

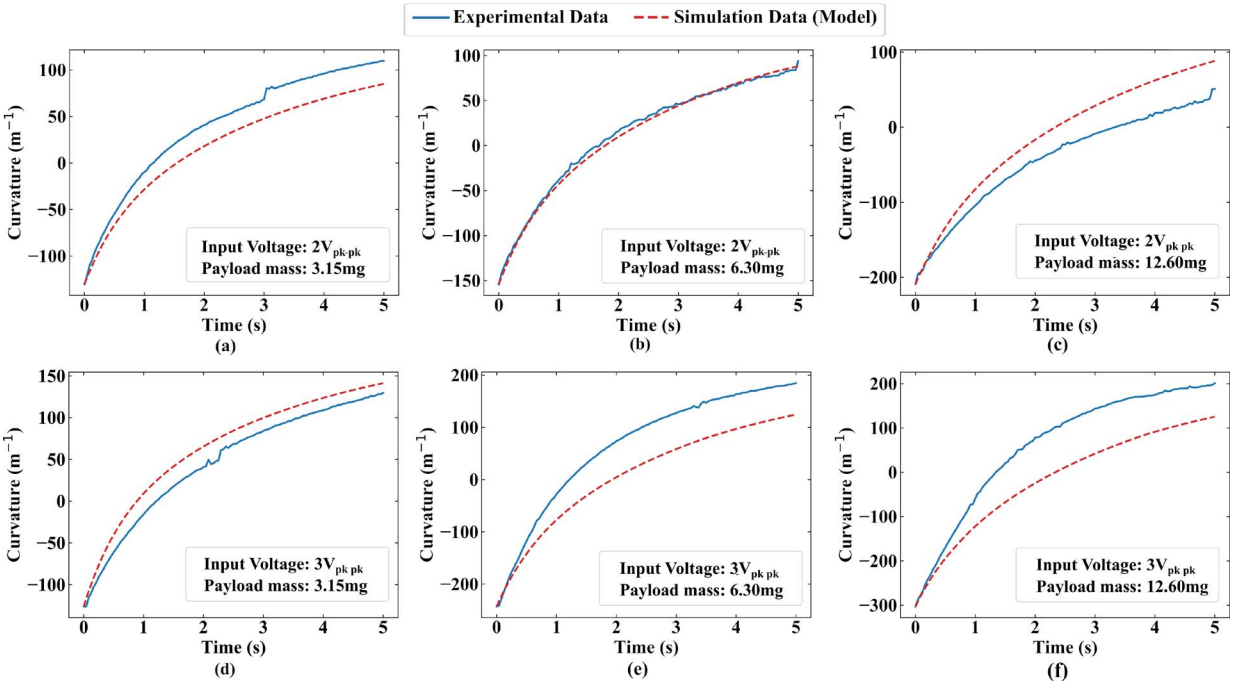

Fig. 7. Concurrence of experimental measurements with simulation results (model). Input voltage amplitudes– Up: 2 V_{pk-pk}, with payload masses (a) 3.15 mg, (b) 6.30 mg, (c) 12.60 mg; Down: 3 V_{pk-pk}, with payload masses (d) 3.15 mg, (e) 6.30 mg, and (f) 12.6 mg.

the mechanical pole moves towards the origin, and for a payload mass of 20 mg, the actuator is marginally stable. The actuator is not stable for payload masses greater than 20 mg.

IV. Results and Discussion

The frequency-domain analysis approach performed in this paper, in addition to extending the actuator model to include the mass loading effects, facilitates identification of the system and application of the model and deepens the understanding of the actuator behavior. The primary goal of this paper, which is an extension of existing actuator models to analyze loading, is achieved. As the actuators are inherently nonlinear except for small displacements, the validity of the suggested method was expected to be restricted to small curvatures [36], [38]. Additionally, the feedback loop in the mechanical subsystem is nonlinear and was approximated with linear components that are accurate for small angles (i.e., curvatures), adding more constraints to the validity of the model. However, the restrictions are met in a vast area of applications, including most medical applications, such as microcatheters, otoscopes, and other minimally invasive devices that require small deflections through tortuous areas to inspect the region of interest [45],[44], [49].

Nevertheless, the approach shows less than a 15% peak-to-peak (P-P) convergence error with the conducted experiments (Fig. 7). In Fig. 7(c), in addition to the errors rooted in nonlinearity deflections due to large curvatures, the domination of the mechanical input over the electrical input magnifies the role of the mass moment of inertia that was neglected in this paper. Neglecting this term leads to a higher convergence error of 14%. It should also be noted that Region 3 is the fastest region, whereas Regions 1 and 5 are the slowest regions. Therefore, when the model has a greater slope at the beginning, it reaches Region 2 sooner. In this case, the model, which overestimated the actuator curvature, is transferred to a region with even more speed when the actuator is in a lower speed region. Thus, the error increases. In contrast, in Fig. 7(a), (e), and (f), the model underestimates the actuator curvature. Therefore, the model remains in Region 1 (e.g., slow region), while the actuator functions in Regions 2 and 3 (faster and fastest regions), leading to a higher (P-P) convergence error. Experiments conducted with 2 V_{pk-pk} and 6.30 mg (see Fig. 7(b)) and 3 V_{pk-pk} and 3.15 mg (see Fig. 7(d)) had (P-P) errors of 2% and 5%, respectively, with the simulation results. Table III shows the (P-P) curvature and error for the experimental measurements and analytical simulations.

Along with the intended goal, the frequency-domain model analysis introduces numerous advantages to IEAP actuator analysis over the conventional time-domain models, to name a few:

- *Actuator-specific model generation*: Time-domain gray-box models require two sets of electrical and mechanical measurements to identify the system. In the frequency domain, however, the actuator's response to a Heaviside step function is enough to obtain the transfer function.
- *Application*: Mathematical calculations in the frequency domain are straightforward. For example, calculating the system response for different inputs and initial conditions with a known transfer function is performed by multiplication, whereas in the time domain, it requires convolution.
- *Model interpretation*: In the frequency domain, information on systems and signals is more concise. Each signal is represented by its frequency component and corresponding amplitude. Systems are defined by zeros, poles, and gain. Therefore, more information about the

system is obtained from its frequency-domain transfer function rather than the time domain. For instance, utilizing Bode diagrams on the actuator used in this work, one can say that as the zero in the transfer function is further from the origin than the closest pole and that the poles are far enough from each other such that the so-called back relaxation effect does not occur in this actuator. One can also determine the maximum working frequency of an actuator for the desired gain and compare different actuators more easily using their transfer functions. Frequency-domain stability analysis could also be utilized.

- *Consistency*: The presented Laplace-domain model is more compatible with models implementing cooperating electromechanical systems, which are usually defined in the Laplace domain.

V. Conclusion

In this paper, micro-ionic polymer actuator (PEDOT:PSS/PEO) model is described in the frequency domain, based on a linear electrochemomechanical model. The mass loading effect was investigated with respect to the proposed linear approach and then established with simulations. Finally, the experimental validation was assessed and compared with the simulation results showing good agreement.

Overall, the novelty of this work lies in modeling the behavior of mass-loaded micro-IEAPs by applying feedback theory in the Laplace domain. Compared to previous similar works on modeling IEAPs, the simplicity and conciseness of the reported approach ease model interpretation, such as analyzing the stability of the system and acquiring key actuator specifications. This technique, which accelerates the generation of actuator-specific models and simplifies its application, is expected to serve as an effective approach towards implementation in potential medical devices.

The proposed linear model reduces the overall computational cost. However, for applications requiring higher precision and fewer constraints on computation power, the same approach could be implemented on a nonlinear actuator model as a potential future extension of this work. By applying nonlinear control theory and including the second moment of inertia, the accuracy can be improved at the cost of the complexity of the control system.

Additionally, we also propose to develop a controlled system addressing the space and integration constraints. In this context, we refer to the reported approach [28] to fabricate microactuators and microsensors based on PEDOT:PSS. Therefore, to sense the deflection, a sensor will be coupled with the actuator to obtain its deformation, the deformation being proportional to the output voltage of the sensor.

Finally, future work will include simulation and experimental validation of closed-loop control for the proposed model to implement these actuators in biomedical applications.

References

[1] D. Rus and M. T. Tolley, "Design, fabrication and control of soft robots," *Nature*, vol. 521, no. 7553, pp. 467–475, May 2015, doi: 10.1038/nature14543.

[2] Q. Shen *et al.*, "Basic design of a biomimetic underwater soft robot with switchable swimming modes and programmable artificial muscles," *Smart Mater. Struct.*, vol. 29, no. 3, Mar. 2020, Art. no. 035038, doi: 10.1088/1361-665X/ab6fe8.

[3] Z. J. Olsen and K. J. Kim, "Design and modeling of a new biomimetic soft robotic jellyfish using IPMC-based electroactive polymers," *Frontiers Robot. AI*, vol. 6, p. 112, Nov. 2019, doi: 10.3389/frobt.2019.00112.

[4] Y. Zhao *et al.*, "Biomimetic beetle-inspired flapping air vehicle actuated by ionic polymer-metal composite actuator," *Appl. Bionics Biomech.*, vol. 2018, Feb. 2018, Art. no. 3091579, doi: 10.1155/2018/3091579.

[5] A. D. Marchese, R. Tedrake, and D. Rus, "Dynamics and trajectory optimization for a soft spatial fluidic elastomer manipulator," *Int. J. Robot. Res.*, vol. 35, no. 8, pp. 1000–1019, Jul. 2016, doi: 10.1177/0278364915587926.

[6] C. D. Onal and D. Rus, "Autonomous undulatory serpentine locomotion utilizing body dynamics of a fluidic soft robot," *Bioinspiration Biomimetics*, vol. 8, no. 2, Mar. 2013, Art. no. 026003, doi: 10.1088/1748-3182/8/2/026003.

[7] F. Carpi and E. Smela, Eds., *Biomedical Applications of Electroactive Polymer Actuators*. Chichester, U.K.: Wiley, 2009.

[8] N. Bhat and W.-J. Kim, "Precision force and position control of an ionic polymer metal composite," *Proc. Inst. Mech. Eng., I, J. Syst. Control Eng.*, vol. 218, no. 6, pp. 421–432, Sep. 2004, doi: 10.1177/095965180421800601.

[9] A. D. Santa, A. Mazzoldi, and D. de Rossi, "Steerable microcatheters actuated by embedded conducting polymer structures," *J. Intell. Mater. Syst. Struct.*, vol. 7, no. 3, pp. 292–300, May 1996, doi: 10.1177/1045389x9600700309.

[10] B. K. Fang, M. S. Ju, and C. C. K. Lin, "Development of active guide-wire for cardiac catheterization by using ionic polymer-metal composites," in *Proc. 13th Int. Conf. Biomed. Eng.*, vol. 23, C. T. Lim and J. C. H. Goh, Eds. Berlin, Germany: Springer, 2009, pp. 340–343.

[11] I. Must, P. Rinne, F. Krull, F. Kaasik, U. Johanson, and A. Aabloo, "Ionic actuators as manipulators for microscopy," *Frontiers Robot. AI*, vol. 6, p. 140, Dec. 2019, doi: 10.3389/frobt.2019.00140.

[12] H. K. A. Tsai *et al.*, "Development of integrated protection for a miniaturized drug delivery system," *Smart Mater. Struct.*, vol. 16, no. 2, p. S295, 2007, doi: 10.1088/0964-1726/16/2/S14.

[13] E. W. H. Jager, C. Immerstrand, K. H. Peterson, K. E. Magnusson, I. Lundström, and O. Inganäs, "The cell clinic: Closable microvials for single cell studies," *Biomed. Microdevices*, vol. 4, pp. 177–187, Jul. 2002, doi: 10.1023/A:1016092228965.

[14] L. M. Low, S. Seetharaman, K. Q. He, and M. J. Madou, "Microactuators toward microvalves for responsive controlled drug delivery," *Sens. Actuators B, Chem.*, vol. 67, nos. 1–2, pp. 149–160, 2000, doi: 10.1016/S0925-4005(00)00396-8.

[15] E. W. H. Jager, O. Inganäs, and I. Lundström, "Microrobots for micrometer-size objects in aqueous media: Potential tools for single-cell manipulation," *Science*, vol. 288, no. 5475, pp. 2335–2338, 2000, doi: 10.1126/science.288.5475.2335.

[16] K. C. Aw, W. Yu, A. J. McDaid, and S. Q. Xie, "An IPMC driven micropump with adaptive on-line iterative feedback tuning," *Proc. SPIE*, vol. 8409, Apr. 2012, Art. no. 84090I, doi: 10.1117/12.914430.

[17] S. Iplikci, M. Y. Coskun, C. Sancak, M. Itik, and G. Alici, "Hybrid force and position control of a conducting tri-layer electroactive polymer actuator," , vol. 39, no. 3, pp. 288–296, 2017, doi: 10.1177/0142331216659537.

[18] D. Pede, E. Smela, T. Johansson, M. Johansson, and O. Inganäs, "A general-purpose conjugated-polymer device array for imaging," *Adv. Mater.*, vol. 10, no. 3, pp. 233–237, 1998, doi: 10.1002/(SICI)1521-4095(199802)10:3<233::AID-ADMA233>3.0.CO;2-M.

[19] S. Guo, T. Fukuda, and K. Asaka, "A new type of fish-like underwater microrobot," *IEEE/ASME Trans. Mechatronics*, vol. 8, no. 1, pp. 136–141, Mar. 2003, doi: 10.1109/TMECH.2003.809134.

[20] A. Khaldi *et al.*, "Conducting interpenetrating polymer network sized to fabricate microactuators," *Appl. Phys. Lett.*, vol. 98, no. 16, 2011, Art. no. 164101, doi: 10.1063/1.3581893.

[21] F. Hu, Y. Xue, J. Xu, and B. Lu, "PEDOT-based conducting polymer actuators," *Frontiers Robot. AI*, vol. 6, p. 114, Nov. 2019, doi: 10.3389/frobt.2019.00114.

[22] C. Plesse, F. Vidal, H. Randriamahazaka, D. Teyssié, and C. Chevrot, "Synthesis and characterization of conducting interpenetrating polymer networks for new actuators," *Polymer*, vol. 46, no. 18, pp. 7771–7778, 2005, doi: 10.1016/j.polymer.2005.03.103.

[23] H. He *et al.*, "Biocompatible conductive polymers with high conductivity and high stretchability," *ACS Appl. Mater. Interfaces*, vol. 11, no. 29, pp. 26185–26193, 2019, doi: 10.1021/acsami.9b07325.
[24] C. A. Cutler, M. Bouguettaya, and J. R. Reynolds, "PEDOT polyelectrolyte based electrochromic films via electrostatic adsorption," *Adv. Mater.*, vol. 14, no. 9, pp. 684–688, 2002, doi: 10.1002/1521-4095(20020503)14:9<684::AID-ADMA684>3.0.CO;2-7.
[25] A. Khaldi *et al.*, "Patterning highly conducting conjugated polymer electrodes for soft and flexible microelectrochemical devices," *ACS Appl. Mater. Interfaces*, vol. 10, no. 17, pp. 14978–14985, 2018, doi: 10.1021/acsami.8b01059.
[26] E. Smela, "Conjugated polymer actuators for biomedical applications," *Adv. Mater.*, vol. 15, no. 6, pp. 481–494, 2003, doi: 10.1002/adma.200390113.
[27] N. T. Nguyen *et al.*, "Microfabricated PEDOT trilayer actuators: Synthesis, characterization, and modeling," *Proc. SPIE*, vol. 10163, Apr. 2017, Art. no. 101631K, doi: 10.1117/12.2260431.
[28] L. Seurre *et al.*, "Demonstrating full integration process for electroactive polymer microtransducers to realize soft microchips," in *Proc. IEEE 33rd Int. Conf. Micro Electro Mech. Syst. (MEMS)*, Jan. 2020, pp. 917–920, doi: 10.1109/MEMS46641.2020.9056371.
[29] L. J. Goujon *et al.*, "Flexible solid polymer electrolytes based on nitrile butadiene rubber/poly (ethylene oxide) interpenetrating polymer networks containing either LiTFSI or EMITFSI," *Macromolecules*, vol. 44, no. 24, pp. 9683–9691, 2011, doi: 10.1021/ma201662h.
[30] K. Rohtlaid, G. T. M. Nguyen, C. Soyer, E. Cattan, F. Vidal, and C. Plesse, "Poly(3,4-ethylenedioxythiophene):Poly(styrene sulfonate)/polyethylene oxide electrodes with improved electrical and electrochemical properties for soft microactuators and microsensors," *Adv. Electron. Mater.*, vol. 5, no. 4, 2019, Art. no. 1800948, doi: 10.1002/aelm.201800948.
[31] F. Carpi, "Electromechanically active polymers," *Polym. Int.*, vol. 59, no. 3, pp. 277–278, 2010, doi: 10.1002/pi.2790.
[32] J. G. Martinez and T. F. Otero, "Mechanical awareness from sensing artificial muscles: Experiments and modeling," *Sens. Actuators B, Chem.*, vol. 195, pp. 365–372, May 2014, doi: 10.1016/j.snb.2013.12.099.
[33] J. D. Madden, "Conducting polymer actuators," Ph.D. dissertation, Massachusetts Inst. Technol., Cambridge, MA, USA, 2000.
[34] S. W. John, G. Alici, and C. D. Cook, "Inversion-based feedforward control of polypyrrole trilayer bender actuators," *IEEE/ASME Trans. Mechatronics*, vol. 15, no. 1, pp. 149–156, Feb. 2010, doi: 10.1109/TMECH.2009.2020732.
[35] Y. Fang, X. Tan, and G. Alici, "Robust adaptive control of conjugated polymer actuators," *IEEE Trans. Control Syst. Technol.*, vol. 16, no. 4, pp. 600–612, Jul. 2008, doi: 10.1109/TCST.2007.912112.
[36] M. Bentefrit *et al.*, "Linear finite-difference bond graph model of an ionic polymer actuator," *Smart Mater. Struct.*, vol. 26, no. 9, Sep. 2017, Art. no. 095055, doi: 10.1088/1361-665X/aa7f7f.
[37] W. Borutzky, *Bond Graph Modelling of Engineering Systems*. 2011.
[38] N. T. Nguyen *et al.*, "Nonlinear dynamic modeling of ultrathin conducting polymer actuators including inertial effects," *Smart Mater. Struct.*, vol. 27, no. 11, 2018, Art. no. 115032, doi: 10.1088/1361-665X/aae456.
[39] M. Farajollahi *et al.*, "Characterization and dynamic charge dependent modeling of conducting polymer trilayer bending," *Smart Mater. Struct.*, vol. 25, no. 11, 2016, Art. no. 115044, doi: 10.1088/0964-1726/25/11/115044.
[40] A. Punning, U. Johanson, M. Anton, A. Aabloo, and M. Kruusmaa, "A distributed model of ionomeric polymer metal composite," *J. Intell. Mater. Syst. Struct.*, vol. 20, no. 14, pp. 1711–1724, 2009, doi: 10.1177/1045389X09337170.
[41] V. Vunder, A. Punning, and A. Aabloo, "Mechanical interpretation of back-relaxation of ionic electroactive polymer actuators," *Smart Mater. Struct.*, vol. 21, no. 11, Nov. 2012, Art. no. 115023, doi: 10.1088/0964-1726/21/11/115023.
[42] G. Nishida, K. Takagi, B. Maschke, and T. Osada, "Multi-scale distributed parameter modeling of ionic polymer-metal composite soft actuator," *Control Eng. Pract.*, vol. 19, no. 4, pp. 321–334, 2011, doi: 10.1016/j.conengprac.2010.10.005.
[43] A. Mattioni, Y. Wu, H. Ramirez, Y. Le Gorrec, and A. Macchelli, "Modelling and control of an IPMC actuated flexible structure: A lumped port Hamiltonian approach," *Control Eng. Pract.*, vol. 1010, Aug. 2020, Art. no. 104498, doi: 10.1016/j.conengprac.2020.104498.
[44] T. Shoa, J. D. Madden, N. R. Munce, and V. Yang, "Analytical modeling of a conducting polymer-driven catheter," *Polym. Int.*, vol. 59, no. 3, pp. 343–351, 2010, doi: 10.1002/pi.2783.
[45] G. Alici, B. Mui, and C. Cook, "Bending modeling and its experimental verification for conducting polymer actuators dedicated to manipulation applications," *Sens. Actuators A, Phys.*, vol. 126, no. 2, pp. 396–404, 2006, doi: 10.1016/j.sna.2005.10.020.
[46] O. Katsuhiko, *Modern Control Engineering*. Upper Saddle River, NJ, USA: Prentice-Hall, 2010.
[47] Phantom. (Aug. 2012). *Phantom Miro Digital High-Speed Cameras*. Datasheet. [Online]. Available: https://www.magic-h.com/images/stories/MIRO_M-LC_Series.pdf
[48] High Speed Vision GmbH. *High Brightness LED Lighting 'Onboard' Version*. Datasheet. Accessed: Nov. 26, 2020. [Online]. Available: https://www.hsvision.de/en/component/phocadownload/category/2-downloads-en?download=56:synclamp-4432-en
[49] M. Runciman, A. Darzi, and G. P. Mylonas, "Soft robotics in minimally invasive surgery," *Soft Robot.*, vol. 6, no. 4, pp. 423–443, Aug. 2019, doi: 10.1089/soro.2018.0136.

Iman Dadras received the B.S. and M.S. degrees in electronic engineering from the Shahid Rajayi Teacher Training University, Tehran, Iran, in 2014 and 2017, respectively. He is currently pursuing the Ph.D. degree with the University of Tartu.

From 2014 to 2017, he worked on wide-band and low-noise transimpedance amplifiers for optical links. Since 2019, he has been working on ASIC design implementation for soft robots. His current research interests include analog and mixed-signal IC design, front-end amplifiers, radio frequency circuits, analog computing, neural network accelerators, soft robotics, and image processing for biomedical applications.

Sofiane Ghenna received the engineer's degree in electrical engineering from the National Polytechnic School of Algiers in 2011, the master's degree in electrical engineering systems from the National Polytechnic Institute - ENSEEIHT Toulouse in 2012, and the Ph.D. degree in electrical engineering from Lille University, France, in 2016.

After one year as a Temporary Teaching and a Research Assistant at Lille University and two years as a Post-Doctoral Researcher at the Centrale-Supélec, Paris, he is currently an Associate Professor with the Université Polytechnique Hauts-de-France, Valenciennes, France. His research interests include modeling and control of smart material-based actuators.

Sébastien Grondel received the M.S. and Ph.D. degrees in electronic and mechanical engineering from the Université Polytechnique Hauts-de-France, France, in 1997 and 2000, respectively. From 2001 to 2010, he worked as a Research Associate with the Electronic, Microelectronic and Nanoelectronic Department, Université Polytechnique Hauts-de-France, focusing on structural health monitoring and medical acoustic imaging. Since 2011, he has been a Professor with the Electronic, Microelectronic and Nanoelectronic Department, and a Teacher with the Engineering School INSA Hauts-de-France. He has contributed to the design and development of the "OVMI" nanoflying insect as well as new ionic polymer actuators. He has authored more than 100 published journal and conference papers related to smart materials, ultrasonication, and mechatronics. His current research interests include modeling, simulation, and control of macro- and micromechatronic systems using the bond graph methodology. He is also an Elected Member of the National Research Evaluation in electronics fields (CNU 63) and belongs to the editorial board of the journal Micromachines. He is also a Fellow of the French Acoustical (SFA) and Electronic, Electrotechnic and Automatic (EEA) Societies.

Éric Cattan received the Ph.D. degree from University Paris XI, Orsay, in 1993. He was then recruited as an Associate Professor with the Laboratory of Advanced Ceramic Materials in 1994. He then joined the Institute of Electronics and Microelectronics and Nanotechnologies, University of Polytechnic Hauts de France, and he became a Professor in 2002. His career began in the field of piezoelectric and ferroelectric thin films, and the last 12 years have been devoted to bioinspired MEMS. In particular, he has focused on the production of an insect-like flying nanodrone fabricated using microfabrication technologies and transducers related to artificial muscles to produce flexible microsystems for the medical field.

Jaan Raik received the M.Sc. and Ph.D. degrees in computer engineering from the Tallinn University of Technology in 1997 and 2001, respectively. He is currently a Professor of Digital Systems Verification with the Department of Computer Systems, Tallinn University of Technology. He is also the Leader of the Center for Dependable Computing Systems Design (DCSD). He has coauthored more than 200 scientific publications. He is also a member of the IEEE Computer Society and HiPEAC, and a member of steering/program committees for several conferences.

Alvo Aabloo (Member, IEEE) received the Ph.D. degree in physics in 1994 focusing on computational research of celluloses. His postdoc research topic was computational modeling of ion exchange polymer membranes in ion-polymer batteries. Since 2004, he has been focusing on ion-polymer active materials (artificial muscles), cross-disciplinary research, computational methods, fabrication, control, and applications. He has successfully supervised 16 Ph.D. students. He has published more than 290 scientific articles, H-index 39 (Google Scholar). Citations 2632 (Scopus), and 3333(Google Scholar). He has been the Coordinator of the H2020 MSCA-ITN network and a Research Partner for FP7, H2020, ESA, EIT-Health, and IT manufacturing projects. His research interests include electrochemomechanically active polymer composite materials, computational materials, ion-polymer batteries, robotics, and space applications.

Saoni Banerji received the M.Sc. degree in electronics from Nanyang Technological University (NTU), Singapore, in 2014, and the Ph.D. degree in electronics engineering from the Universitat Politècnica de Catalunya (UPC), Barcelona, Spain, in 2017, with an FI AGAUR grant from the Catalonian government in the fields of microelectromechanical systems (MEMS) design and circuits and designing control architectures for MEMS sensor signal conditioning. After the completion of her Ph.D., she worked in a CMOS-MEMS startup, Nanusens, as a Simulation and Characterization Engineer from 2017 to 2018. In 2018, she joined the University of Tartu, Tartu, Estonia, as a Research Fellow of microfabrication and microtechnology. Here, she works towards designing and characterizing microsystems by integrating CMOS electronics with ionic electroactive polymer (IEAP) sensors dedicated to medical technologies. Her current research interests and competencies include integrating electronics in soft fiber sensors and actuators dedicated to medical and wearable applications, MEMS modeling, design of signal conditioning architectures with CMOS processes, and testing and characterization of CMOS-MEMS devices.